JACS
JOURNAL OF THE AMERICAN CHEMICAL SOCIETY
Article
pubs.acs.org/JACS

# Synthesis and Catalytic Properties of Metal Clusters Encapsulated within Small-Pore (SOD, GIS, ANA) Zeolites

Sarika Goel, Zhijie Wu,[†] Stacey I. Zones,[‡] and Enrique Iglesia*

Department of Chemical and Biomolecular Engineering, University of California at Berkeley, Berkeley, California 94720, United States

Supporting Information

**ABSTRACT:** The synthesis protocols for encapsulation of metal clusters reported here expand the diversity in catalytic chemistries made possible by the ability of microporous solids to select reactants, transition states, and products on the basis of their molecular size. We report a synthesis strategy for the encapsulation of noble metals and their oxides within SOD (Sodalite, 0.28 nm × 0.28 nm), GIS (Gismondine, 0.45 nm × 0.31 nm), and ANA (Analcime, 0.42 nm × 0.16 nm) zeolites. Encapsulation was achieved via direct hydrothermal synthesis for SOD and GIS using metal precursors stabilized by ammonia or organic amine ligands, which prevent their decomposition or precipitation as colloidal hydroxides at the conditions of hydrothermal synthesis (<380 K) and favor interactions between metal precursors and incipient aluminosilicate nuclei during self-assembly of microporous frameworks. The synthesis of ANA requires higher crystallization temperatures (~415 K) and high pH (>12), thereby causing precipitation of even ligand-stabilized metal precursors as hydroxides. As a result, encapsulation was achieved by the recrystallization of metal clusters containing GIS into ANA, which retained these metal clusters within voids throughout the GIS−ANA transformation.

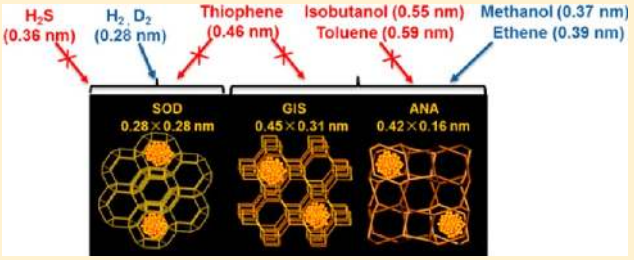


## INTRODUCTION

Encapsulation of metal and oxide clusters within zeolites[1−5] can protect such clusters against sintering and also prevent their contact with toxic impurities, while concurrently allowing active sites to select reactants and transition states on the basis of molecular size.[6−10] The confinement of such clusters within small-pore zeolites (<0.45 nm apertures) cannot be achieved via post-synthesis exchange from aqueous or vapor media, because the size of cationic or anionic precursors, with their charge-balancing double layer, and of gaseous complexes prevents their diffusion through the apertures in these microporous aluminosilicates. In these materials, encapsulation requires that precursors be placed and retained within microporous frameworks during hydrothermal syntheses and subsequent thermal treatment.[9,11] The high pH (>12) conditions required for hydrothermal crystallization of zeolites typically cause the precipitation of such precursors as colloidal metal hydroxides larger than the zeolite voids,[12] thus preventing their encapsulation. Organic amines and $NH_3$ ligands can stabilize metal cations and prevent premature precipitation; they can also act as coordinating agents to encourage the sequestering of precursors during the incipient formation of aluminosilicate frameworks.[13]

Hydrothermal synthesis of zeolites proceeds via three steps: induction, nucleation, and crystallization.[14] The framework building units are denoted as the "host" and the external component as the "guest". Zeolite nucleation and crystallization hinges on a balance of guest−host assembly with the guest stabilizing the surrounding zeolite framework.[15] The ligand-stabilized metal cationic complexes used here are hydrophilic and are very effective in templating Al-rich zeolites (Sodalite (SOD), Analcime (ANA), and Gismondine (GIS))[16] during hydrothermal synthesis, in contrast with Si-rich zeolites, which require hydrophobic organo-cations as stabilizing guests and structure-directing agents.[17]

We present here synthetic protocols for the encapsulation of active metals within zeolites with small voids (SOD, GIS, and ANA, Figure 1) and show that such zeolite structures can protect Pt, Pd, Ru, and Rh clusters against sintering and from contact with larger molecules that block active surfaces. These data also provide chemical and structural evidence for

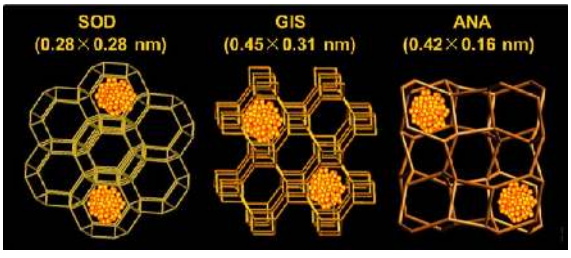


**Figure 1.** Pictorial representation of metal clusters encapsulated within zeolites and zeolite aperture sizes.

**Received:** July 26, 2012
**Published:** September 27, 2012

   dx.doi.org/10.1021/ja307370z | J. Am. Chem. Soc. 2012, 134, 17688−17695

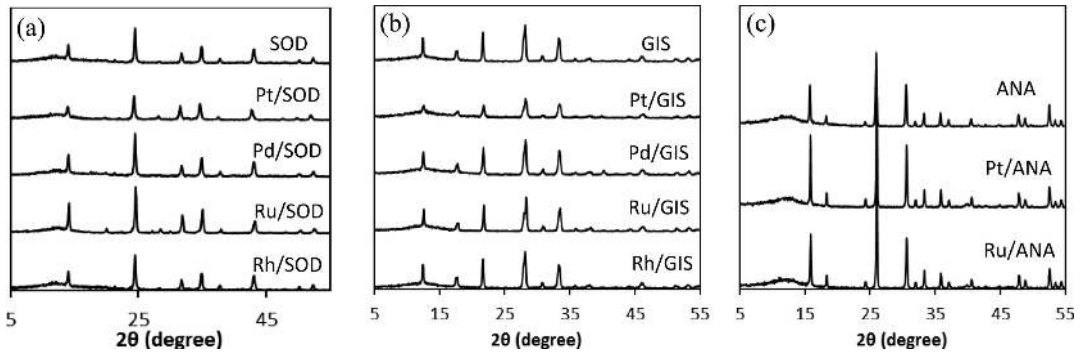


**Figure 2.** X-ray diffraction patterns of (a) M/SOD, (b) M/GIS, and (c) M/ANA samples (M = Pt, Pd, Ru, Rh).

confinement and for the consequences of encapsulation on catalytic rates and selectivity. Precursor stabilization during synthesis proved infeasible for ANA because of the high temperatures required for its crystallization (~415 K). GIS structures already containing reduced metal clusters were instead converted into ANA via local recrystallization processes that retained metal clusters within ANA crystals.

Encapsulation and phase purity were established using X-ray diffraction, transmission electron microscopy, and titration methods. Oxidative dehydrogenation (ODH) of methanol (kinetic diameter 0.37 nm) and isobutanol (kinetic diameter 0.55 nm), hydrogenation of ethene (kinetic diameter 0.39 nm) and toluene (kinetic diameter 0.59 nm), and ethene hydrogenation in the presence and absence of thiophene (kinetic diameter 0.46 nm) were used to confirm encapsulation and to establish the ability of metal-containing GIS and ANA catalysts to select reactants on the basis of size and to protect active sites from large organosulfur poisons. $H_2$–$D_2$ (kinetic diameter 0.28 nm) isotopic exchange in the presence and absence of $H_2S$ (kinetic diameter 0.36 nm) was used to probe the ability of metal-containing SOD to activate dihydrogen without interference by $H_2S$.

## ■ RESULTS AND DISCUSSION

The direct encapsulation of metal precursors during hydrothermal synthesis requires interactions between metal precursors and incipient aluminosilicate frameworks, which are favored by cationic metal complexes because of the anionic nature of aluminosilicate building blocks.[11] Encapsulation requires the self-assembly of these building blocks around solvated cations.[12] At the high pH (>12) of hydrothermal syntheses, these cations precipitate prematurely as colloidal hydroxides (Supporting Information Table S1, precipitation time for metal precursors in alkaline solution) that cannot be contained within the voids in incipient aluminosilicate frameworks, thus preventing encapsulation. Ammonia and ethylene diamine ligands stabilize cationic precursors and prevent their precipitation, even at higher pH (up to ~13) and temperatures above ambient (up to ~390 K). Additionally, these ligands can act as tethers between cationic complexes and the emerging aluminosilicate moieties that ultimately assemble into zeolite frameworks, thus favoring the inclusion of metal precursors within SOD and GIS zeolite voids as they form. ANA requires higher temperature (~415 K) for crystallization, which leads to rapid formation of metal hydroxides even when metal precursors are stabilized by ligands (Figure S1, Supporting Information). The synthesis of ANA involves the initial formation of GIS, which then converts to ANA.[18] These observations led us to attempt the recrystallization of metal encapsulated within GIS (M/GIS) into metal encapsulated within ANA (M/ANA) while retaining metal clusters within crystallites.

**Structural Evidence for Zeolite Phase and for Confinement and Surface Cleanliness of Metal and Oxide Clusters.** X-ray diffraction (XRD) patterns for metal-containing zeolites (M/SOD, M/GIS, and M/ANA) (Figure 2) showed lines corresponding to crystalline forms of the intended zeolite structures, indicating that ligated precursors did not interfere with hydrothermal crystallization processes. Transmission electron micrographs (TEM) for M/GIS and high-angle annular dark-field scanning transmission electron micrographs (HAADF STEM) (Figure 3) after reduction of precursors and passivation of metal clusters showed that they were present as small clusters uniform in size and distributed throughout zeolite crystallites. The metal clusters in SOD were not visible by TEM, but HAADF STEM images show the presence of small clusters (1.0–1.5 nm, Figure 3) in Pt/SOD.

$H_2$ uptakes gave metal dispersions of 0.63–0.70 for Pt, Pd, Ru, and Rh clusters in GIS, 0.50–0.61 for Pt and Ru in ANA, and 0.22–0.39 for Pt, Pd, Ru, and Rh in SOD (Table 1) after thermal treatment at 573 K. The dispersion values obtained from $H_2$-chemisorption in SOD samples are small compared to the values expected on the basis of electron microscopy due to the limited access of even hydrogen to active sites tightly contained within small aperture SOD cages. The agreement between surface-averaged mean diameters from electron micrographs in M/GIS (M = Pt, Pd, Ru, and Rh) and Pt/ANA and those determined from $H_2$ chemisorption uptakes (assuming spherical clusters; Figure 3) indicates that all clusters detectable by microscopy exhibit clean surfaces accessible to these titrants and that the ligands present during hydrothermal synthesis are removed by the thermal treatments used. We conclude from these data that metal cluster surfaces are available for catalytic reactions of any reactants that can diffuse through the microporous frameworks in GIS and ANA zeolites at rates commensurate with those of the surface-catalyzed chemical reactions.

**Catalytic Evidence for Encapsulation: Oxidative Dehydrogenation of Methanol and Isobutanol and Hydrogenation of Ethene and Toluene on GIS- and ANA-Supported Catalysts.** The molecular dimensions of GIS and ANA apertures allow them to sieve reactants and products on the basis of size, while the intervening intracrystal voids can stabilize specific transition states that maximize their van der Waals contacts with the framework. Oxidative dehydrogenation (ODH) rates of methanol[19] and isobutanol


dx.doi.org/10.1021/ja307370z | J. Am. Chem. Soc. 2012, 134, 17688–17695

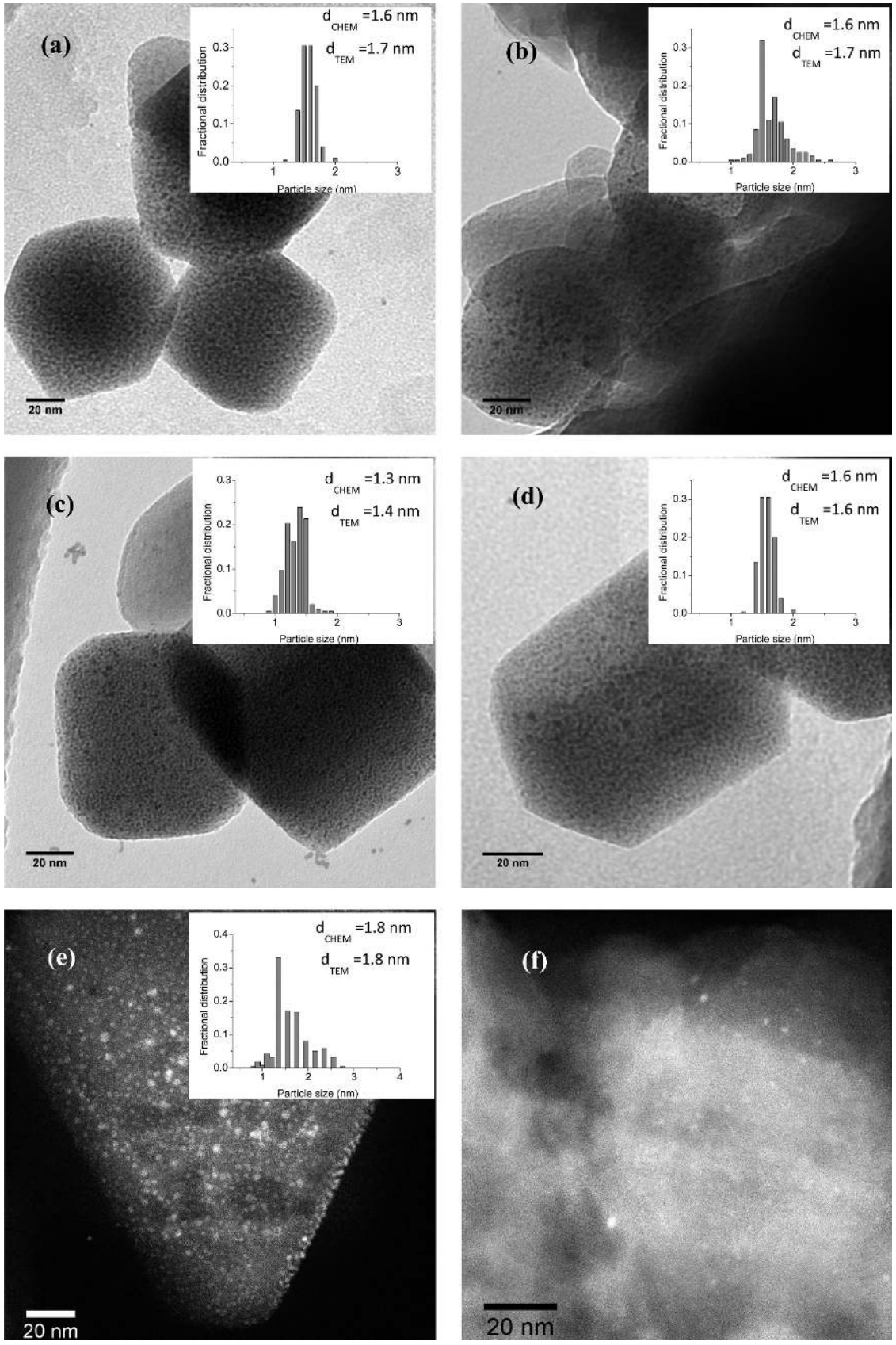


**Figure 3.** Metal clusters size distributions and TEM images of (a) Pt/GIS, (b) Pd/GIS, (c) Ru/GIS, (d) Rh/GIS, and HAADF STEM images of (e) Pt/ANA and (f) Pt/SOD samples. Surface-weighted metal cluster size diameters, $d_{TEM}$, were calculated using $d_{TEM} = \sum n_i d_i^3 / \sum n_i d_i^2$. Metal clusters size distribution is not included for Pt/SOD because it was difficult to locate enough platinum clusters to be able to get a statistical value for average cluster size.


dx.doi.org/10.1021/ja307370z | J. Am. Chem. Soc. 2012, 134, 17688−17695

**Table 1. Metal Precursors, Loadings, and Dispersions of Metal Clusters (Pt, Pd, Ru, Rh) Dispersed in $SiO_2$, SOD, GIS, and ANA Samples**

| sample | precursor used | metal loading[a] (wt %) | metal dispersion[b] (fraction) |
|---|---|---|---|
| $Pt/SiO_2$ | $[Pt(NH_3)_4](NO_3)_2$ | 0.79 | 0.61 |
| $Pd/SiO_2$ | $[Pd(NH_3)_4](NO_3)_2$ | 0.55 | 0.69 |
| $Ru/SiO_2$ | $[Ru(NH_3)_6]Cl_3$ | 0.50 | 0.50 |
| $Rh/SiO_2$ | $[Rh(NH_3)_5Cl]Cl_2$ | 1.10 | 0.60 |
| Pt/SOD | $[Pt(NH_3)_4](NO_3)_2$ | 0.10 | 0.38 |
| Pd/SOD | $[Pd(NH_2CH_2CH_2NH_2)_2]Cl_2$ | 0.10 | 0.23 |
| Ru/SOD | $[Ru(NH_3)_6]Cl_3$ | 0.034 | 0.22 |
| Rh/SOD | $[Rh(NH_2CH_2CH_2NH_2)_3]Cl_3{\cdot}3H_2O$ | 0.045 | 0.39 |
| Pt/GIS | $[Pt(NH_3)_4](NO_3)_2$ | 0.86 | 0.70 |
| Pd/GIS | $[Pd(NH_2CH_2CH_2NH_2)_2]Cl_2$ | 0.85 | 0.68 |
| Ru/GIS | $[Ru(NH_3)_6]Cl_3$ | 0.40 | 0.63 |
| Rh/GIS | $[Rh(NH_2CH_2CH_2NH_2)_3]Cl_3{\cdot}3H_2O$ | 0.24 | 0.67 |
| Pt/ANA | $[Pt(NH_3)_4](NO_3)_2$ | 1.00 | 0.61 |
| Ru/ANA | $[Ru(NH_3)_6]Cl_3$ | 0.50 | 0.50 |

[a]Analyzed by inductively coupled plasma optical emission spectroscopy. [b]Metal dispersions estimated from $H_2$ chemisorptions.

**Table 2. Catalytic Properties of Metal Clusters (Pt, Pd, Ru, Rh) Dispersed in GIS, ANA, and $SiO_2$ in Oxidative Dehydrogenation of Alkanols[a]**

| sample | $r_{methanol}$[b] (mol-($mol_{surf\text{-}metal}^{-1}$–$s^{-1}$)) | $r_{isobutanol}$[b] (mol-($mol_{surf\text{-}metal}^{-1}$–$s^{-1}$)) | $\chi_{ODH,j}$[c] j = zeolite, $SiO_2$ | $\phi$[d] |
|---|---|---|---|---|
| Pt/GIS | 3.56 | 0.0191 | 186.4 | |
| $Pt/SiO_2$ | 7.02 | 1.45 | 4.8 | 38.5 |
| Pd/GIS | 0.20 | 0.0104 | 19.4 | |
| $Pd/SiO_2$ | 0.51 | 0.23 | 2.2 | 8.8 |
| Ru/GIS | 0.13 | 0.0017 | 76.4 | |
| $Ru/SiO_2$ | 0.05 | 0.04 | 1.2 | 70.0 |
| Rh/GIS | 0.17 | 0.0016 | 107.6 | |
| $Rh/SiO_2$ | 0.19 | 0.15 | 1.3 | 82.7 |
| Pt/ANA | 0.33 | 0.0021 | 160.9 | |
| $Pt/SiO_2$ | 7.02 | 1.45 | 4.8 | 33.2 |
| Ru/ANA | 0.02 | 0.0003 | 66.6 | |
| $Ru/SiO_2$ | 0.05 | 0.04 | 1.2 | 55.5 |

[a]Alkanol oxidative dehydrogenation reactions were carried out with 4 kPa alkanols and 9 kPa $O_2$ at 393 K. [b]Reaction turnover rate is defined as mole of reactant converted per mol of surface metal atoms per second. [c]$\chi_{ODH,j} = r_{methanol}/r_{isobutanol}$, j = zeolite, $SiO_2$. [d]$\phi = \chi_{ODH,zeolite}/\chi_{ODH,SiO_2}$.

**Table 3. Catalytic Properties of Pt Dispersed in GIS, ANA, and $SiO_2$ in Hydrogenation of Ethene[a] and Toluene[b]**

| sample | $r_{ethene}$[c] (mol-($mol_{surf\text{-}metal}^{-1}$–$s^{-1}$)) | $r_{toluene}$[c] (mol-($mol_{surf\text{-}metal}^{-1}$–$s^{-1}$)) | $\chi_{HYD,j}$[d] j = zeolite, $SiO_2$ | $\phi$[e] |
|---|---|---|---|---|
| Pt/GIS | 2.90 | 0.012 | 241.6 | |
| $Pt/SiO_2$ | 5.26 | 1.38 | 3.8 | 63.4 |
| Pt/ANA | 2.00 | 0.011 | 181.8 | |
| $Pt/SiO_2$ | 5.26 | 1.38 | 3.8 | 47.7 |

[a]Ethene hydrogenation reactions were carried out with 0.95 kPa ethene and 5 kPa $H_2$ at 308 K . [b]Toluene hydrogenation reactions were carried out with 0.35 kPa toluene, 99.65 kPa $H_2$ at 473 K. [c]Reaction turnover rate is defined as mole of reactant converted per mole of surface metal atoms per second. [d]$\chi_{HYD,j} = r_{ethene}/r_{toluene}$, j = zeolite, $SiO_2$. [e]$\phi = \chi_{HYD,zeolite}/\chi_{HYD,\ SiO_2}$.

(0.37 and 0.55 nm respective kinetic diameters) and hydrogenation of ethene and toluene (0.39 and 0.59 nm respective kinetic diameters) were used to confirm the predominant presence of Pt, Pd, Ru, and Rh clusters within GIS (0.45 nm × 0.31 nm aperture) and of Pt and Ru clusters within ANA (0.42 nm × 0.16 nm aperture). Methanol and ethene, but not isobutanol and toluene, can access sites encapsulated within GIS or ANA zeolite crystals via diffusion through their interconnected voids and apertures.

The selectivity of encapsulation processes during hydrothermal synthesis was assessed by first measuring the ratio of ODH and hydrogenation rates for the small and large reactants on unconstrained clusters dispersed on $SiO_2$ ($\chi_{ODH,SiO_2} = r_{methanol}/r_{isobutanol}$, $\chi_{HYD,SiO_2} = r_{ethene}/r_{toluene}$) to determine the relative reactivity of these two molecules on unconstrained systems; similar data for the same metal in zeolite samples ($\chi_{i,zeolite}$, i = ODH, HYD) allow the ratio of these relative reactivities to be expressed as an encapsulation selectivity parameter ($\phi = \chi_{i,zeolite}/\chi_{i,SiO_2}$, i = ODH, HYD) for each reaction and reactant pair. This ratio represents a direct measure of the diffusional constraints imposed on larger reactants by the presence of metal clusters within zeolite structures; it is therefore a rigorous indicator of the extent to


dx.doi.org/10.1021/ja307370z | J. Am. Chem. Soc. 2012, 134, 17688–17695

which the active surfaces are contained within the microporous networks. This encapsulation selectivity parameter would approach unity for clusters with unimpeded access to reactants, such as those at external zeolite surfaces. Values of $\phi$ provide the functional definition of the effectiveness of synthetic protocols, as well as the mechanistic and practical manifestation of reactant shape selectivity; values larger than ~5 are taken here as evidence of successful encapsulation.

M/GIS and M/ANA samples gave much larger $\chi_{ODH,zeolite}$ and $\chi_{HYD,zeolite}$ values than the respective metals dispersed on $SiO_2$ (Tables 2 and 3) and high encapsulation selectivities ($\phi$ = 8−83, Figure 4) for both ODH and hydrogenation reactions,

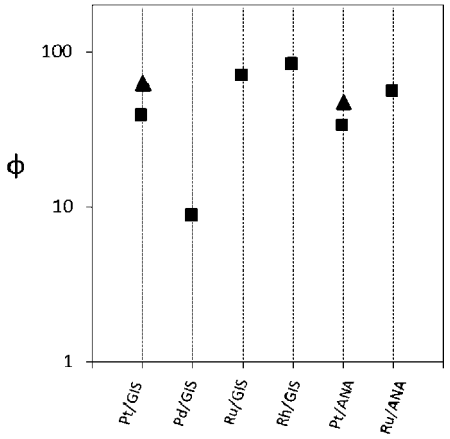


**Figure 4.** Encapsulation selectivity parameter ($\phi$), reflecting the shape selectivity for various M/GIS and M/ANA samples (M = Pt, Pd, Ru, Rh) in alkanol oxidative dehydrogenation (ODH) (■) and ethene and toluene hydrogenation (▲). $\phi$ values larger than unity indicate the preferential containment of clusters within zeolite micropores that can sieve reactants on the basis of size.

indicating that active sites on these zeolites indeed reside predominantly within locations accessible only to the smaller methanol and ethene reactants. Methanol ODH and ethene hydrogenation turnover rates (per exposed metal atom determined from chemisorption uptakes) were smaller on metals dispersed on GIS and ANA than on $SiO_2$, indicating that even for small ethene and methanol molecules access to active surface is restricted by diffusion through the zeolite aperture or by limited access to the active clusters tightly contained within zeolite cages.

**Catalytic Evidence for the Protection of Active Sites from Large Sulfur Poisons: Hydrogenation of Ethene in the Presence and Absence of Thiophene in GIS- and ANA-Supported Catalysts.** The diffusional constraints that restrict access to active sites by larger reactants also serve to prevent contact between encapsulated metal clusters and larger organosulfur poisons, such as thiophene, which titrate surface atoms and render them unreactive. These expectations were confirmed by measuring ethene (0.39 nm kinetic diameter) hydrogenation rates on Pt/GIS and Pt/ANA and on the respective metals dispersed on $SiO_2$ in the presence or absence of thiophene (0.46 nm kinetic diameter; 0.4 kPa) (Figure 5), an organosulfur titrant that cannot readily diffuse through the small apertures in GIS and ANA.

The addition of thiophene (0.4 kPa) to the reactants decreased ethene hydrogenation rates by a factor of 13 in Pt/GIS, 7 in Pt/ANA, and 530 in Pt/$SiO_2$. After thiophene addition was stopped, ethene hydrogenation rates recovered to

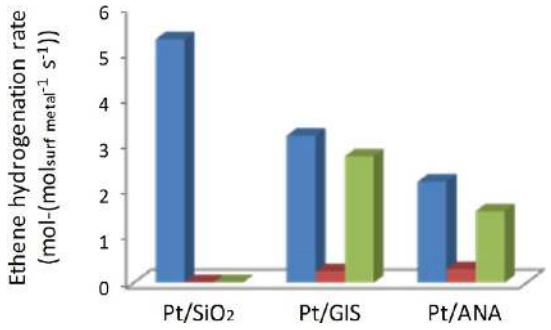


**Figure 5.** Ethene hydrogenation rate in Pt/$SiO_2$, Pt/GIS, and Pt/ANA samples without thiophene (blue), with 0.4 kPa thiophene added for 1 h (red), and after stopping thiophene injection (green). Ethene hydrogenation reaction was carried out with 0.95 kPa ethene, 5 kPa $H_2$, and 0 kPa/0.4 kPa thiophene at 315 K. Reaction turnover rate is defined as ethene hydrogenation rate per mol of surface metal atoms per second.

0.85 of initial rate in Pt/GIS and 0.70 in Pt/ANA (Figure 5). In sharp contrast, metal clusters dispersed on $SiO_2$ did not show any detectable increase in hydrogenation rates after removal of thiophene from ethene-$H_2$ feed. The lower rates observed on Pt/ANA and Pt/GIS after thiophene addition appear to reflect the combined effects of titration of external clusters and diffusional constraints on ethene reactants imposed by thiophene physisorbed on external zeolite surfaces and blocking the zeolite aperture; the latter effects are reversible and disappear upon removal of thiophene.

The essential retention of ethene hydrogenation rates for metal clusters on GIS and ANA zeolites after stopping thiophene confirms that 0.70−0.85 fraction of the active metal cluster surfaces resides within GIS and ANA structures, where such active sites cannot contact the organosulfur compound.

**Evidence of Encapsulation and Protection of Active Sites from Toxic Sulfur Compounds: $H_2$−$D_2$ Exchange Rates on SOD-Supported Catalysts.** The smaller apertures in SOD (0.28 nm) allow the diffusion of $H_2$ (0.28 nm kinetic diameter) and $D_2$ (0.28 nm kinetic diameter), but few other molecules.[20] The protection of active sites from $H_2S$ (0.36 nm kinetic diameter) was demonstrated by measuring $H_2$−$D_2$ exchange rates at 373 K in the absence and presence of $H_2S$ (1 kPa) on Pt, Pd, Ru, and Rh clusters dispersed on SOD and the same metal clusters dispersed on $SiO_2$.

The addition of $H_2S$ to $H_2$−$D_2$ decreased $H_2$−$D_2$ exchange rates by a factor of 2.7−9.9 on $SiO_2$-supported metals, as expected from the titration of exposed surface atoms by sulfur moieties derived from $H_2S$. In contrast, isotopic exchange rates decreased by much smaller factors (1.3−1.5) on M/SOD samples when $H_2S$ (1 kPa) was present in $H_2$−$D_2$ reactants (Figure 6). Residual $H_2$−$D_2$ exchange rates on $SiO_2$-supported clusters in the presence of $H_2S$ (Figure 6) reflect exchange rates on S-containing surfaces, including exchange between H-atoms from $H_2S$ and D-atoms in $D_2$. $H_2S$ inhibition of exchange rates in M/SOD reflects the combined effects of irreversible titration of external clusters by chemisorbed sulfur species and reversible $H_2S$ physisorption at external SOD surfaces, which interferes with the diffusion of dihydrogen isotopes. The latter effect is reversible upon removal of $H_2S$ from the $H_2$−$D_2$ reactants and leads to the partial recovery of exchange rates (Figure 6). The residual rates after $H_2S$ removal rigorously reflect the rates on encapsulated surfaces on M/SOD samples never exposed to


dx.doi.org/10.1021/ja307370z | J. Am. Chem. Soc. 2012, 134, 17688−17695

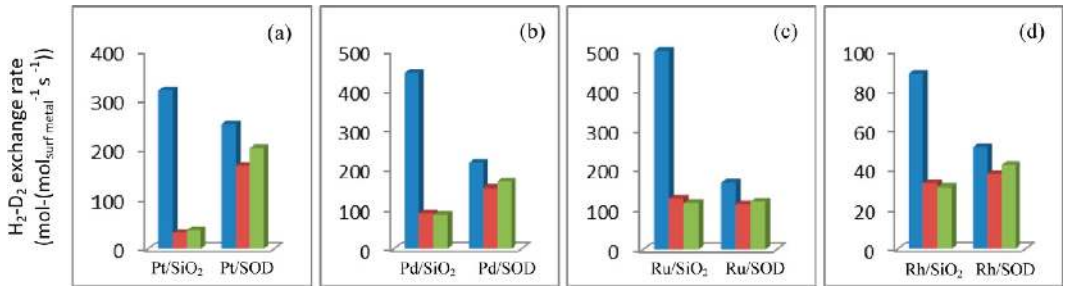


**Figure 6.** $H_2-D_2$ exchange rate in (a) Pt, (b) Pd, (c) Ru, and (d) Rh clusters dispersed on $SiO_2$ and SOD without $H_2S$ (blue), with 1.0 kPa $H_2S$ added for 1 h (red), and after stopping $H_2S$ injection (green). $H_2-D_2$ exchange reactions were carried out with 50.05 kPa $H_2$, 49.95 kPa $D_2$, and 0 kPa/1 kPa $H_2S$ at 373 K. Reaction turnover rate is defined as $H_2-D_2$ exchange rate per mol of surface metal atoms per second.

$H_2S$. $H_2S$ removal from $H_2-D_2$ did not lead to any changes in exchange rates on unprotected clusters dispersed on $SiO_2$, because inhibition reflects only the titration of active metal surfaces without additional contributions from diffusional effects.

The exchange rates on M/SOD were corrected by rates measured on $M/SiO_2$ in the presence of $H_2S$ to obtain the rate coming solely from $H_2-D_2$ exchange on metal clusters encapsulated within SOD framework. These calculations show that a large fraction of the active surfaces (0.64−0.79 fraction) are protected from $H_2S$ in M/SOD samples, apparently because such surfaces reside within SOD crystals that are inaccessible to $H_2S$. These data show that encapsulated clusters within SOD can be effectively protected against all sulfur poisons, while concurrently demonstrating the high encapsulation selectivity achieved.

**Practical Implications.** Metal clusters encapsulated within ANA and GIS provide practical catalysts for the selective hydrogenation−dehydrogenation of linear hydrocarbons and oxygenates over branched or cyclic analogues as evidenced from selective oxidative dehydrogenation of methanol and isobutanol and selective hydrogenation of ethene and toluene (Figure 4). These catalysts can also effectively prevent inhibition of these reactions by larger and more strongly bound species, such as arenes and organosulfur compounds, as evidenced by the protection of active sites from thiophene poisons in ethene hydrogenation (Figure 5). The SOD-encapsulated clusters can potentially extract $H_2$ via dissociative adsorption from streams containing $H_2S$ at ambient temperatures and subsequent desorption during temperature cycling. These materials reversibly chemisorb $H_2$ (Table 1) and retain their ability to do so in the presence of $H_2S$ during $H_2-D_2$ exchange reactions (Figure 6).

## CONCLUSION

Encapsulation of noble metals (Pt, Pd, Ru, and Rh) was achieved within small-pore zeolites (SOD and GIS) via direct hydrothermal synthesis using ligands that prevent precipitation as colloidal hydroxides at the high pH required for zeolite crystallization. ANA-encapsulated clusters were prepared by post-synthesis recrystallization of their metal-containing GIS analogues, because the high temperature required for direct ANA synthesis decomposed even ligand-protected metal precursors. The relative rates of oxidative dehydrogenation of methanol and isobutanol and of hydrogenation of ethene and toluene on metals clusters in GIS, ANA, and $SiO_2$ and the similar cluster sizes inferred from chemisorption and TEM show that surfaces of metal clusters are clean and reside predominantly with GIS and ANA, where they are accessible only to the smaller reactants. These conclusions were further confirmed by the ability of these materials to catalyze ethene hydrogenation in the presence of thiophene poisons. Thus, metal clusters encapsulated within ANA and GIS provide effective catalysts for the selective hydrogenation−dehydrogenation of reactants smaller than zeolite apertures over larger ones while protecting the active surfaces from large organosulfur poisons, which irreversibly bind the active surfaces. $H_2-D_2$ exchange rates in the presence of $H_2S$ were much higher on M/SOD than on $M/SiO_2$, consistent with preferential encapsulation of metal clusters within voids protected from $H_2S$, making these materials potentially useful to extract $H_2$ via dissociative adsorption from sulfur-contaminated streams.

## EXPERIMENTAL SECTION

**Materials.** Fumed $SiO_2$ (0.014 $\mu$m, 200 ± 25 $m^2$ $g^{-1}$, Sigma), $NaAlO_2$ (anhydrous, Riedel-de Haën, technical), NaOH (99.995%, Aldrich), $[Pd(NH_2CH_2CH_2NH_2)_2]Cl_2$ (99.9%, Aldrich), $[Pd(NH_3)_4](NO_3)_2$ (10 wt % in water, Aldrich), $[Pt(NH_3)_4](NO_3)_2$ (99.99%, Alfa Aesar), $[Rh(NH_3)_5Cl]Cl_2$ (Rh 34.5% min, Alfa Aesar), $[Rh(NH_2CH_2CH_2NH_2)_3]Cl_3{\cdot}3H_2O$ (≥99.5%, Aldrich), $[Ru(NH_3)_6]Cl_3$ (98%, Aldrich), methanol ($CH_3OH$, 99.9%, Aldrich), isobutanol (i-$C_4H_9OH$, 99.9%, Aldrich), toluene (≥99.9%, Aldrich), He (99.999%, Praxair), $H_2$ (99.999%, Praxair), $D_2$ (99.999%, Praxair), $H_2-D_2$ mixture (50.05% $H_2$, 49.95% $D_2$, Praxair, certified mixture), $H_2S$ (0.5% $H_2S/H_2$, Praxair, certified mixture), ethene (5% $C_2H_4$/He, Praxair, CS), and thiophene (99%, Aldrich) were used as received.

**Synthesis.** Gels with molar composition of $20Na_2O:1.0Al_2O_3:1.5SiO_2:160H_2O$ for SOD and $5.5Na_2O:1.0Al_2O_3:4.0SiO_2:190H_2O$ for GIS were prepared. $NaAlO_2$ and NaOH were dissolved in demineralized $H_2O$ and mixed with fumed $SiO_2$. Metal precursors $[Pt(NH_3)_4](NO_3)_2$, $[Rh(NH_2CH_2CH_2NH_2)_3]Cl_3{\cdot}3H_2O$, or $[Ru(NH_3)_6]Cl_3$ were dissolved in 10 $cm^3$ $H_2O$ and added dropwise to the gel at 0.0833 $cm^3$ $s^{-1}$. The gel was transferred into a 125 $cm^3$ polypropylene container (Nalgene), sealed, and homogenized by vigorous magnetic stirring for 600 s. These gels were stirred in an oil bath at 400 rpm and 373 K for 7 h for SOD and 363 K for 3 d for GIS. The solids were collected on a fritted funnel (Pyrex 36060, 10−15 $\mu$m) and washed with deionized water until the rinse liquid reached pH 7−8. The sample was treated in ambient air at 373 K overnight, then heated in air (1.667 $cm^3$ $g^{-1}$ $s^{-1}$) at 623 K (0.0333 K $s^{-1}$) for 3 h, and treated in 9% $H_2$/He (1.667 $cm^3$ $g^{-1}$ $s^{-1}$, Praxair) at 573 K (0.0333 K $s^{-1}$) for 2 h. Samples were passivated under 0.5% $O_2$/He (1.667 $cm^3$ $g^{-1}$ $s^{-1}$, Praxair) for 1 h at ambient temperature before air exposure.

The successful encapsulation of Pd clusters into SOD and GIS required initially dispersed ligand stabilized metal precursors over the $SiO_2$ surface. $[Pd(NH_2CH_2CH_2NH_2)_2]Cl_2$ was first dissolved in deionized water, and then fumed $SiO_2$ was added to the mixture. The resulting mixture was stirred at 400 rpm and 333 K for 3 h. Next, a solution of NaOH and $NaAlO_2$ was added and stirred at 400 rpm and


dx.doi.org/10.1021/ja307370z | J. Am. Chem. Soc. 2012, 134, 17688−17695

333 K for 1 h. The slurry temperature was raised to the crystallization temperature of the respective zeolite, and the slurry was stirred at 400 rpm. Subsequent steps were the same as for the encapsulation of Pt, Ru, and Rh in SOD and GIS.

The procedures described above were unsuccessful in the synthesis of M/ANA zeolite because the high temperatures required for ANA synthesis decomposed the metal precursors to colloidal hydroxides. Instead, M/ANA samples were prepared by adding NaOH (9 mL $g(M/GIS)^{-1}$) to a previously prepared M/GIS sample, and the mixture was placed within a sealed polypropylene container. The mixture was magnetically stirred at 400 rpm for 1 h, transferred to and recrystallized in a Teflon-lined stainless steel autoclave under static conditions at 413 K for 3 d. The resulting solids were washed, dried, and treated using the procedures reported above for M/GIS samples.

The metal clusters supported on $SiO_2$ (Davisil, grade 646, 300 $m^2$ $g^{-1}$) were prepared by the incipient wetness impregnation method using aqueous solutions of the metal precursors shown in Table 1. Silica-supported samples were dried and treated using the same procedures as zeolite-supported samples.

**Physical Characterization.** The identity and phase purity of zeolites and the absence of large metal structures were demonstrated by X-ray diffraction (Cu K$\alpha$ radiation $\lambda$ = 0.15418 nm, Siemens, D500). Fractional metal dispersions were determined by hydrogen chemisorption using an Autosorb-1 titration apparatus (Quantachrome). Samples were heated to 623 K at 0.0333 K $s^{-1}$ in flowing $H_2$ (Praxair, 99.999%, 0.2 $cm^3$ $s^{-1}$ $g^{-1}$) and held for 1 h and then evacuated for 1 h at 623 K to remove any chemisorbed hydrogen. Dispersions were determined from difference of total and irreversible $H_2$ uptakes using a 1:1 $H:M_{surface}$ adsorption stoichiometry.[21] Hydrogen adsorption isotherms were measured at 313 K and 5−50 kPa of $H_2$ for Pt, Ru, and Rh samples and at 343 K and 0.4−1.5 kPa of $H_2$ for Pd samples to prevent formation of bulk $\beta$-hydrides in Pd samples.[22] Transmission electron microscopy (TEM) images were taken with a Philips 420 TEM operated at 120 kV. Before TEM investigation, the samples were embedded into an adhesive polymer, mechanically thinned, and dimpled and further thinned by Ar ion-milling (Gatan PIP Precision Ion Polishing System, 3.0 kV). High-angle annular dark-field scanning electron microscopy (HAADF STEM) images were taken with JEOL 2100 AC (aberration-corrected). Before imaging, samples were embedded and microtomed using a diamond knife to approximate thickness of 70 nm. Particle size distributions were determined by counting at least 200 crystallites in the micrographs of each sample. The surface area weighted cluster diameters, $d_{TEM}$, were calculated using $d_{TEM} = \sum n_i d_i^3 / \sum n_i d_i^2$ [23] and compared to average particle diameter calculated from hydrogen chemisorption measurements to confirm the accessibility of the surface of all clusters and complete removal of ligands.

**Catalytic Rate Measurements.** Oxidative dehydrogenation (ODH) of alkanols, ethene and toluene hydrogenation, and $H_2-D_2$ exchange rates were measured on catalyst samples diluted with fumed $SiO_2$ (Cab-O-Sil, HS-5, 310 $m^2$ $g^{-1}$) using a quartz reactor with plug-flow dynamics. Dilution was achieved by intimate mixing at a diluent/catalyst mass ratio of 10 and pelleting and sieving the granules to retain aggregates of 0.18−0.25 mm diameter, 5−25 mg sample of which was then mixed with acid-washed quartz granules of similar size (Fluka, acid-purified, 1.0 g) to avoid intrapellet and bed gradients in concentration or temperature. Prereduced and passivated samples were treated in flowing $H_2$ (1.667 $cm^3$ $g^{-1}$ $s^{-1}$) by heating to 573 K at 0.0333 K $s^{-1}$ and holding for 1 h before measuring hydrogenation and $H_2-D_2$ exchange rates and in 20% $O_2$/He flow at 393 K for 1 h before oxidation rate measurements. Alkanol oxidation rates were measured with 4 kPa of alkanol, 9 kPa of $O_2$, and 87 kPa of He as diluent at 393 K, toluene hydrogenation at 0.35 kPa of toluene, 99.65 kPa of $H_2$ at 473 K, and ethene hydrogenation at 0.95 kPa of ethene, 5 kPa of $H_2$, 94 kPa of He as diluent, and 0/0.4 kPa of thiophene at 308/315 K. $H_2-D_2$ exchange rates were measured using an equimolar $H_2-D_2$ mixture (50.05 kPa $H_2$, 49.95 kPa $D_2$) and 0/1.0 kPa of $H_2S$ at 373 K. Rates are reported as turnover rates, defined as the number of molecules converted per time normalized by the number of surface metal atoms determined from chemisorption measurements. Reactant and product concentrations in oxidation and hydrogenation reactions were measured by gas chromatography (Agilent 6890GC) using a methyl−silicone capillary column (HP-1; 50 m × 0.25 mm, 0.25 $\mu$m film thickness) and a Porapak Q packed column (80−100 mesh, 1.82 m × 3.18 mm) connected to flame ionization and thermal conductivity detectors, respectively. $H_2-D_2$ exchange rates were measured by using online mass spectrometry (Leybold Inficon, Transpector Series). Quartz, fumed $SiO_2$, or metal-free zeolites did not give detectable ODH, hydrogenation, or $H_2-D_2$ exchange rates, and rates on M/zeolites did not depend on extent of dilution or change with reaction time.

## ■ ASSOCIATED CONTENT

### Supporting Information

TEM image showing bulk platinum precipitation in direct hydrothermal synthesis of ANA and stability of metal precursors in alkaline solution. This material is available free of charge via the Internet at http://pubs.acs.org.

## ■ AUTHOR INFORMATION


### Corresponding Author

iglesia@berkeley.edu

### Present Addresses

[†]China University of Petroleum, Beijing 102249, China.
[‡]Chevron Energy Technology Company, Richmond, California 94804, United States.


### Notes

The authors declare the following competing financial interest(s): (1) The funding for the research came from Chevron Energy and Technology Co. (2) Stacey I. Zones is an employee of this company and then more generally also a stockholder from Chevron Corp.

## ■ ACKNOWLEDGMENTS

We thank Dr. Alex Kuperman for technical input and advice, Dr. George D. Meritnez for the technical review of the manuscript, Thomas Rea for HAADF imaging, and Chevron Energy Technology for the financial support of this research.

## ■ REFERENCES


(1) Gallezot, P. *Post-Synthesis Modification I* **2002**, 257.
(2) Sachtler, W. M. H. *Acc. Chem. Res.* **1993**, *26*, 383.
(3) Guczi, L.; Kiricsi, I. *Appl. Catal., A* **1999**, *186*, 375.
(4) Zhan, B.-Z.; Iglesia, E. *Angew. Chem., Int. Ed.* **2007**, *46*, 3697.
(5) Zhan, B.-Z.; White, M. A.; Sham, T. K.; Pincock, J. A.; Doucet, R. J.; Rao, K. V. R.; Rao, Robertson, K. N.; Cameron, T. S. *J. Am. Chem. Soc.* **2003**, *125*, 2195.
(6) Csicsery, S. M. *Zeolites* **1984**, *4*, 202.
(7) Weisz, P. B.; Frilette, V. J.; Maatman, R. W.; Mower, E. B. *J. Catal.* **1962**, *1*, 307.
(8) Creyghton, E.; Downing, R. *J. Mol. Catal. A: Chem.* **1998**, *134*, 47.
(9) Altwasser, S.; Gläser, R.; Weitkamp, J. *Microporous Mesoporous Mater.* **2007**, *104*, 281.
(10) Yang, H.; Chen, H.; Chen, J.; Omotoso, O.; Ring, Z. *J. Catal.* **2006**, *243*, 36.
(11) Balkus, K. J.; Gabrielov, A. G. *J. Inclusion Phenom. Mol. Recognit. Chem.* **1995**, *21*, 159.
(12) Choi, M.; Wu, Z.; Iglesia, E. *J. Am. Chem. Soc.* **2010**, *132*, 9129.
(13) Wu, Z.; Choi, M.; Iglesia, E., unpublished results.
(14) Cundy, C. S.; Cox, P. A. *Microporous Mesoporous Mater.* **2005**, *82*, 1.
(15) Barrer, R. M. *Zeolite Synthesis*; American Chemical Society: Washington, DC, 1989; Vol. *398*, p 11.
(16) International Zeolite Association. *Atlas of Zeolite Framework Types*; http://iza-online.org.

(17) Zones, S. I. *J. Chem. Soc., Faraday Trans.* **1991**, *87*, 3709.
(18) Kohoutkova, M.; Klouzkova, A.; Maixner, J.; Mrazova, M. *Ceram.-Silik.* **2007**, *51*, 9.
(19) Liu, H.; Iglesia, E. *J. Phys. Chem. B* **2005**, *109*, 2155.
(20) Weitkamp, J.; Fritz, M.; Ernst, S. *Int. J. Hydrogen Energy* **1995**, *20*, 967.
(21) Bergeret, G.; Gallezot, P. *Handbook of Heterogeneous Catalysis*; Wiley-VCH Verlag GmbH & Co. KgaA: New York, 2008.
(22) Aben, P. *J. Catal.* **1968**, *10*, 224.
(23) Schneider, M.; Duff, D.; Mallat, T.; Wildberger, M.; Baiker, A. *J. Catal.* **1994**, *147*, 500.